CrossMark

Changes in Photospheric Lorentz Force in Eruptive and Confined Solar Flares

Samriddhi Sankar Maity[1,2] , Ranadeep Sarkar[3] , Piyali Chatterjee[1] , and Nandita Srivastava[4]
[1] Indian Institute of Astrophysics, Bangalore, India
[2] Joint Astronomy Programme and Department of Physics, Indian Institute of Science, Bangalore, India
[3] University of Helsinki, Finland; ranadeep.sarkar@helsinki.fi
[4] Udaipur Solar Observatory, Physical Research Laboratory, Udaipur, India

Abstract

Solar flares are known to leave imprints on the magnetic field in the photosphere, often manifested as an abrupt and permanent change in the downward-directed Lorentz force in localized areas inside the active region. Our study aims to differentiate eruptive and confined solar flares based on the variations in vertical Lorentz force. We select 26 eruptive and 11 confined major solar flares (stronger than the GOES M5 class) observed during 2011–2017. We analyze these flaring regions using SHARP vector magnetograms obtained from NASA's Helioseismic and Magnetic Imager. We also compare data corresponding to two synthetic flares from a δ-sunspot simulation reported by Chatterjee et al. We estimate the change in the horizontal magnetic field and the total Lorentz force integrated over an area around the polarity inversion line (PIL) that encompasses the location of the flare. Our results indicate a rapid increase in the horizontal magnetic field along the flaring PIL, accompanied by a significant change in the downward-directed Lorentz force in the same vicinity. Notably, we find that all the confined events under study exhibit a total change in Lorentz force of $<1.8 \times 10^{22}$ dyn. This threshold plays an important role in effectively distinguishing eruptive and confined flares. Further, our analysis suggests that the change in total Lorentz force also depends on the reconnection height in the solar corona at the associated flare onset. The results provide significant implications for understanding the flare-related upward impulse transmission for the associated coronal mass ejection.

1. Introduction

Solar flares and coronal mass ejections (CMEs) are considered the two most violent and energetic phenomena occurring in the solar atmosphere due to the sudden release of energy. A typical flare is distinguished by a quick increase in light emission over a broad range of the electromagnetic spectrum that affects the solar atmosphere, while a CME consists of plasma and high-energy particles that are expelled from the Sun. They are responsible for significant space weather impacts on Earth (Siscoe 2000; Baker et al. 2004; Chen 2017; Green et al. 2018). Therefore, understanding the characteristics of the source region of these energetic solar events has become one of the most important goals of space science research (Sarkar et al. 2024). Solar flares in relation to CMEs are classified into two types: eruptive and confined (Moore et al. 2001). Eruptive flares are associated with CMEs, while confined flares do not have associated CMEs.

Previous observations have shown that flares and CMEs are different manifestations of the same energy-release process (Zhang et al. 2001; Harrison 2003). Moreover, Zhang et al. (2001) have shown that the phase of rapid acceleration of CMEs in the inner corona is temporarily correlated with the rise time of the associated soft X-ray flares. In spite of the intrinsic correlation between flares and CMEs, observations have shown that not all flares are associated with CMEs (Andrews 2003; Yashiro et al. 2005; Yashiro & Gopalswamy 2009; Webb &

Howard 2012; Youssef 2012). Active regions (ARs) with complex topology are the primary sources of large flares and most energetic CMEs (Zirin & Liggett 1987; Sammis et al. 2000; Yang et al. 2017). During a flaring event, the magnetic field reorganizes rapidly in the corona owing to the low Alfvén travel time, leading to the eruption of a magnetic flux rope and the subsequent formation of postflare loops beneath the current sheet, in accordance with the standard flare model (Carmichael 1964; Sturrock 1966; Hirayama 1974; Kopp & Pneuman 1976; Shibata & Magara 2011). The flaring process converts the magnetic free energy into kinetic, thermal, and nonthermal energy that accelerates particles. Although the photosphere is much denser than the corona, the photospheric magnetic field can respond to sudden coronal restructuring during flaring events (Wang & Liu 2015; Aulanier 2016; Toriumi & Wang 2019). Counterintuitively, observations have shown that the photospheric magnetic field does experience significant changes during flares (Wang & Liu 2015; Toriumi & Wang 2019; Kumar & Kumar 2020). Since there is no practical or direct method to measure the vector magnetic field in the coronal volume, it is challenging to quantitatively investigate the temporal evolution of nonpotential parameters (e.g., magnetic free energy) (Wiegelmann et al. 2014). Therefore, the temporal or spatial evolution of parameters in the source region that can only be estimated from the photospheric (Petrie & Sudol 2010) and chromospheric (Kleint 2017) magnetic field (e.g., the change in the net Lorentz force) becomes a major probe to study the changes associated with the flare. Hudson et al. (2008) were the first to suggest that photospheric magnetic fields should become more horizontal after the flare due to the effect of vertical Lorentz

forces on the solar surface. Developing this model further, Fisher et al. (2012) gave a practical approach to calculate the net Lorentz force acting on the solar photosphere. They found an increase in the horizontal magnetic field (B_h), particularly around the polarity inversion line (PIL), and an associated large and abrupt downward change in the vertical Lorentz force. Previous studies have also found that large eruptive flares are associated with a sudden downward change in the Lorentz force (Petrie & Sudol 2010; Petrie 2012). In contrast to B_h, the vertical magnetic field (B_z) varies much less during the flare with no clear pattern (Sun et al. 2017). On the other hand, the horizontal gradient of the vertical magnetic field weighted by sunspot area is found to follow a distinct pattern before a flare, providing potential predictive capability (Korsós et al. 2015). This behavior of the weighted gradient is also marked by the approaching–receding motion of the barycenters of opposite polarities before the flare. Sarkar & Srivastava (2018) compared the magnitude of changes in the horizontal magnetic field (B_h) and the net vertical Lorentz force associated with eruptive and confined flares that occurred in the same AR. They reported that the flare-associated changes in magnetic parameters are larger for eruptive flares than for confined ones. Extending the study to large recurrent flares, Sarkar et al. (2019) found that the change in net vertical Lorentz force acts as an excellent proxy to predict recurrent large flaring events from a single AR. Vasantharaju et al. (2022) reported that the changes in vertical Lorentz force during flares near PILs correlate well with the flare strength. However, no clear classification of the association of flares with CMEs has been made to statistically distinguish them by the net change in Lorentz force.

We now have evidence of rapid and permanent changes in the longitudinal and transverse magnetic fields linked to solar flares in the photosphere thanks to the availability of high-cadence photospheric vector magnetograms from ground- and space-based telescopes (Sudol & Harvey 2005; Petrie & Sudol 2010; Gosain 2012; Wang et al. 2012a; Sun et al. 2017; Castellanos Durán et al. 2018; Petrie 2019; Kazachenko et al. 2022; Liu et al. 2022; Kazachenko 2023).

The magnetic implosion conjecture is frequently used to explain observational evidence of the rise in the horizontal component of the magnetic field in the solar atmosphere (Hudson 2000). It states that in an environment of low plasma β, the coronal loops must contract during a transient event, such as a flare or a CME, in order to lower the magnetic energy. According to Hudson et al. (2008) and Fisher et al. (2012), the release of free magnetic energy should be accompanied by a decrease in the magnetic pressure and volume. A magneto-hydrodynamic (MHD) wave that propagates downward toward the photosphere and perturbs the field there may also be excited by this abrupt change in the corona, which increases the horizontal component of the magnetic field in the photosphere near the PIL (Fletcher & Hudson 2008; Hudson et al. 2008; Wheatland et al. 2018). Li et al. (2011) discovered that, following the flare, the horizontal magnetic field close to the flaring PIL shows a change in both observations and simulation.

In this study, we analyzed the photospheric field variations of 37 events by using the 12 minutes cadence vector magnetogram from the Helioseismic and Magnetic Imager (HMI) on board Solar Dynamics Observatory (SDO). We further augment the event list with the addition of the two of four synthetic flares that occurred in the three-dimensional MHD simulation reported in Chatterjee et al. (2016) and Korsós et al. (2018). The primary motivation of this work is to understand the correlation of the change in vertical Lorentz force with the eruptivity of the flares and to uniquely classify flares associated with CMEs in terms of the change in Lorentz force. The rest of the paper is structured as follows. In Section 2, we describe the data set and methods employed. The results are presented in Section 3. Finally, we discuss the results and summarize our conclusions in Section 4.

2. Data and Methods

2.1. Observational Data

Based on the event catalog provided by Jing et al. (2018), we selected 37 major solar flares, consisting of 15 X class and 22 M class, that originated from 26 ARs located within ±45° of the center of the solar disk. The selected events comprise both eruptive and confined flares over a seven-year period from 2011 January 26 to 2017 December 11. For each event, we used the vector magnetograms of the AR during the flaring event obtained by HMI (Schou et al. 2012) on board SDO (Pesnell et al. 2012). In particular, we used the HMI vector magnetogram series from the version of Space Weather HMI Active Region Patches (SHARP, Turmon et al. 2010) that have a spatial resolution of $0.5''$ with a temporal cadence of 12 minutes. HMI measures the Stokes parameters at six wavelengths centered on the Fe I 6173 Å absorption line with a bandwidth of 76 Å. Based on these observations, the photospheric vector magnetic field is derived by inverting the full set of Stokes parameters using the Milne–Eddington inversion approach (Borrero et al. 2011) to obtain the vector magnetic field components in the photosphere. As part of the additional data preprocessing steps, a coordinate transformation is performed to remap the vector fields onto the Lambert cylindrical equal-area projection. Subsequently, the components of the vector field are converted into heliographic coordinates (B_x, B_y, B_z). Apart from the 12 minutes cadence, HMI also has vector magnetic field data with a high temporal cadence of 135 s. However, we carried out our analysis using the 12 minutes cadence vector magnetogram data due to their lower noise level than that of the 135 s cadence for full-disk vector magnetogram data (Sun et al. 2017). Moreover, the flare-related changes in field are sufficiently captured with the cadence of 12 minutes as studied previously (Sarkar & Srivastava 2018; Sarkar et al. 2019).

We have also used the 1600 Å images provided by the Atmospheric Imaging Assembly (AIA, Lemen et al. 2012) on board SDO to approximate the location of flare ribbons, which helps identify and select the region of interest (RoI) on the vector magnetograms. In order to characterize and analyze the evolution of changes in magnetic field, we chose a 12 hr time window around the time of the solar flare, encompassing six hours both before and after the peak of the flare. The start, peak, and end times of the flare are determined from the Hinode catalog.[5]

2.2. Simulation Data

In order to compare the observations with simulation, we focus on the numerical case study presented in Chatterjee et al. (2016) for our analysis. We provide a

---

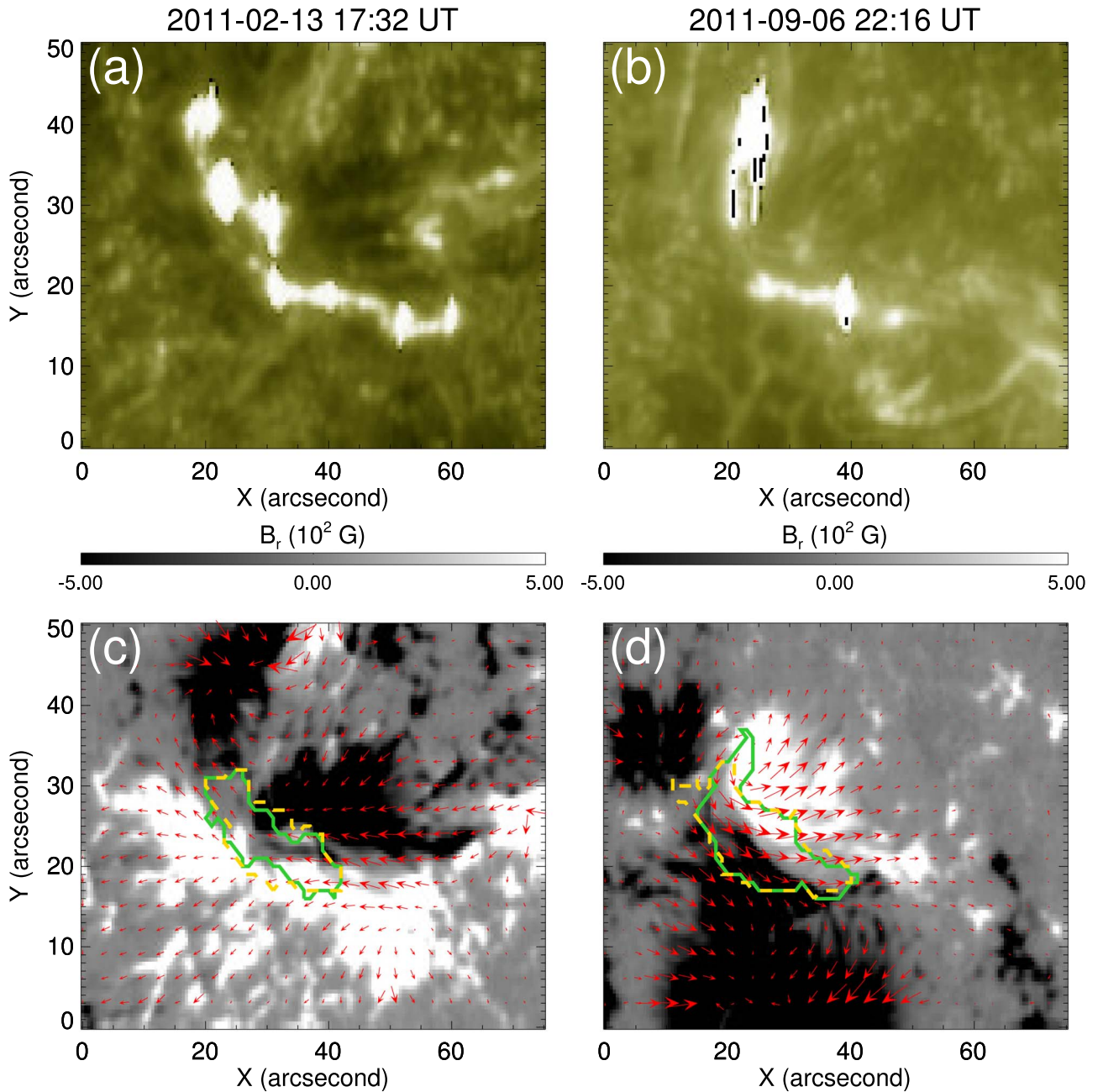[5] https://hinode.isee.nagoya-u.ac.jp/flare_catalogue/

Figure 1. Illustrations of two eruptive events to identify the RoIs of the magnetic imprints. The top panels are AIA 1600 Å images of the two flaring events that occurred on (a) 2011 February 13 at 17:38 UT and (b) 2011 September 6 at 22:20 UT. The bottom panels represent the corresponding vertical magnetic field B_z, whose strength is indicated by color bars. The horizontal component of the magnetic field is shown by the red arrows. The overplotted contours mark the RoIs selected based on the individual difference maps of B_h (yellow dashed line) and F_z (solid green lines).

concise overview of the model setup here for completeness. The box-shaped computational domain has horizontal extents of $-18\,\mathrm{Mm} < x$, $y < 18\,\mathrm{Mm}$ and a vertical one of $-8.5\,\mathrm{Mm} < z < 16.5\,\mathrm{Mm}$, with a uniformly spaced grid with $dx = dy = 96\,\mathrm{km}$ and $dz = 48\,\mathrm{km}$, rotating with an angular velocity similar to the Sun and forming an angle of $30°$ with the vertical z-direction. A constant gravity, g_z, points in the negative z-direction. For the calculation, the authors use the Pencil Code[6] (Pencil Code Collaboration et al. 2021)—a fully compressible higher-order finite difference tool. Beginning from the initial state, the simulation was run for 263 minutes of

solar time. The initial subsurface horizontal magnetic sheet breaks up, rises, and emerges through the surface like a newly emerging AR after about 145 minutes. Four flaring eruptions were recognized. The first two flares in the simulation are B- and C-class with onset times at 167.5 and 197.2 minutes, respectively, and they are analyzed for this work. We excluded the other two flares from the analysis due to the presence of numerical artifacts.

The flares reported in the above work released energies of $\approx 2 \times 10^{31}\,\mathrm{erg}$, commensurate with B- and C-class flares. First of all, note that it is computationally challenging to produce solar flare energies of M and X class in solar MHD simulations with photospheric flux emergence due to the requirement for a
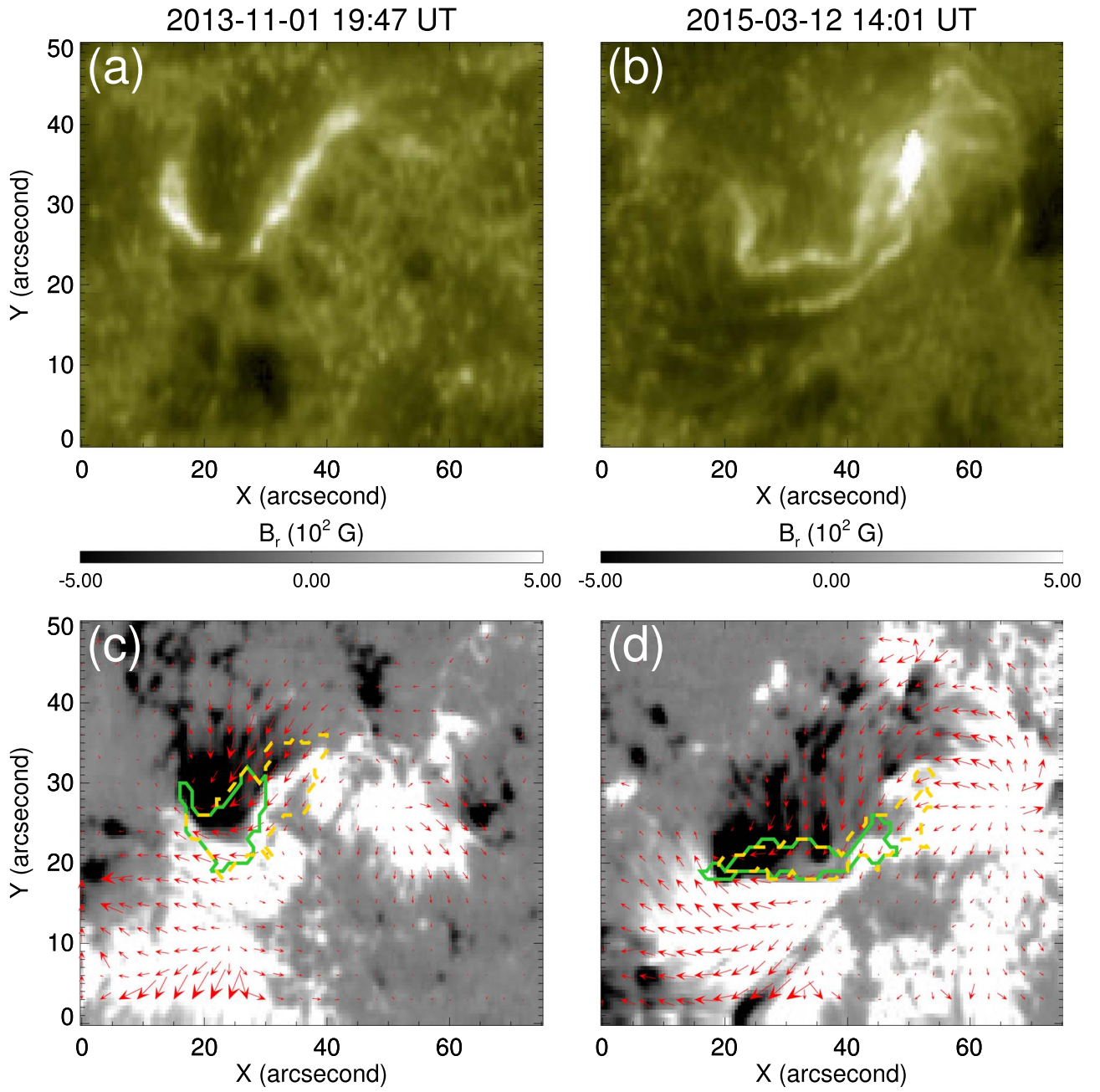
Figure 2. Similar to Figure 1 but for confined events that occurred on (a), (c) 2013 November 1 at 19:53 UT and (b), (d) 2015 March 12 at 14:08 UT.

very high magnetic Reynolds number, domain size, and the wall clock time. Conversely, analyzing stronger flares proves easier in observations, while changes caused by weaker flares might go undetected by current instruments. Kumar & Kumar (2020) and Vasantharaju et al. (2022) incorporated C-class flares in their studies, despite the uncertainty in the vector magnetic field data associated with them. Consequently, we decided to forego additional observational analysis of weak flares, focusing instead on understanding the magnetic imprint problem through numerical simulation. Our approach involves tackling the issue from two contrasting perspectives of variability. We intend to comprehensively understand the problem by examining minor flares through numerical simulation and major flares through observational data.

2.3. Lorentz Force and Masking Algorithm

We utilized the formulation proposed by Fisher et al. (2012) to calculate the total changes in the Lorentz force. The variation in the horizontal and vertical components of the Lorentz force within a time interval δt is computed using the following equations:

$$\delta F_z = \frac{1}{8\pi} \int_{A_{\mathrm{ph}}} (\delta B_h^2 - \delta B_z^2) \, dA \qquad (1)$$

$$\delta F_h = -\frac{1}{4\pi} \int_{A_{\mathrm{ph}}} \delta (B_h B_z) \, dA. \qquad (2)$$

Here B_h and B_z represent the horizontal and vertical components of the magnetic field, respectively, and F_h and

Table 1
List of 37 Flare Events from 27 Active Regions and Their Associated Magnetic Properties

No	Date	Peak Time	NOAA AR	Position	Flare Class	Type[a]	F_z Contour		B_h Contour		Ribbon Distance
							ΔB_h (G)[b]	ΔF_z (dyn)[c]	ΔB_h (G)[b]	ΔF_z (dyn)[c]	(Mm)
1	2011-02-13	17:38:00	11158	S20E04	M6.6	E	293.7 ± 67.1	1.80 ± 0.32	275.6 ± 63.1	1.74 ± 0.33	9.1
2	2011-02-15	01:56:00	11158	S20W10	X2.2	E	192.5 ± 25.5	3.75 ± 0.87	197.8 ± 29.4	3.10 ± 0.88	7.9
3	2011-03-09	23:23:00	11166	N08W09	X1.5	C	293.7 ± 44.1	0.98 ± 0.27	312.1 ± 45.9	0.93 ± 0.22	34.7
4	2011-07-30	02:09:00	11261	S20W10	M9.3	C	287.5 ± 61.1	1.39 ± 0.26	469.7 ± 67.3	1.29 ± 0.19	12.7
5	2011-08-03	13:48:00	11261	N16W30	M6.0	E	341.6 ± 23.4	3.12 ± 0.18	304.5 ± 24.3	2.87 ± 0.21	11.6
6	2011-09-06	01:50:00	11283	N14W07	M5.3	E	222.5 ± 39.3	1.85 ± 0.31	208.0 ± 34.5	2.24 ± 0.47	5.6
7	2011-09-06	22:20:00	11283	N14W18	X2.1	E	370.4 ± 24.2	2.30 ± 0.13	361.2 ± 25.3	2.14 ± 0.11	5.2
8	2011-10-02	00:50:00	11305	N12W26	M3.9	C	190.0 ± 47.1	0.21 ± 0.06	187.5 ± 40.7	0.21 ± 0.10	15.7
9	2012-01-23	03:59:00	11402	N28W21	M8.7	E	316.6 ± 53.2	0.71 ± 0.09	289.7 ± 55.4	0.62 ± 0.12	52.9
10	2012-03-07	00:24:00	11429	N17E31	X5.4	E	215.0 ± 19.4	8.42 ± 0.90	239.5 ± 21.0	8.56 ± 0.96	3.4
11	2012-03-09	03:53:00	11429	N15W03	M6.3	E	233.3 ± 19.6	1.89 ± 0.09	233.6 ± 22.1	1.72 ± 0.17	6.5
12	2012-07-02	10:52:00	11515	S17E08	M5.6	E	263.3 ± 61.5	0.35 ± 0.11	235.2 ± 74.9	0.20 ± 0.05	20.1
13	2012-07-12	16:49:00	11520	S15W01	X1.4	E	225.0 ± 33.8	0.38 ± 0.05	225.1 ± 33.8	0.41 ± 0.05	38.0
14	2013-04-11	07:16:00	11719	N09E12	M6.5	E	385.0 ± 116.6	0.15 ± 0.02	235.3 ± 85.0	0.15 ± 0.01	22.4
15	2013-10-24	00:30:00	11877	S09E10	M9.3	E	264.0 ± 94.0	0.17 ± 0.04	630.2 ± 196.7	0.25 ± 0.07	17.0
16	2013-11-01	19:53:00	11884	S12E01	M6.3	C	338.3 ± 15.9	1.50 ± 0.11	308.3 ± 22.2	1.43 ± 0.14	9.7
17	2013-11-03	05:22:00	11884	S12W17	M4.9	C	335.0 ± 44.1	0.88 ± 0.10	287.9 ± 45.6	0.87 ± 0.20	7.9
18	2013-11-05	22:12:00	11890	S12E44	X3.3	E	379.1 ± 111.3	2.85 ± 0.98	450.4 ± 78.0	2.82 ± 0.98	5.0
19	2013-11-08	04:26:00	11890	S12E13	X1.1	E	425.0 ± 22.9	5.28 ± 0.31	384.3 ± 23.2	5.18 ± 0.33	3.5
20	2014-01-07	18:32:00	11944	S15W11	X1.2	E	90.6 ± 27.4	1.06 ± 0.16	106.6 ± 69.5	0.6 ± 0.12	100.2
21	2014-02-02	09:31:00	11967	S10E13	M4.4	C	286.5 ± 215.1	1.44 ± 1.04	218.7 ± 279.5	0.96 ± 0.48	15.9
22	2014-02-04	04:00:00	11967	S14W06	M5.2	C	166.6 ± 114.9	1.50 ± 0.62	229.2 ± 105.2	1.27 ± 0.32	15.1
23	2014-03-29	17:48:00	12017	N10W32	X1.1	E	402.0 ± 79.0	0.71 ± 0.21	230.9 ± 52.6	1.42 ± 0.40	13.1
24	2014-04-18	13:03:00	12036	S20W34	M7.3	E	161.6 ± 43.4	0.19 ± 0.04	151.9 ± 20.5	0.36 ± 0.13	16.7
25	2014-09-10	17:45:00	12158	N11E05	X1.6	E	122.0 ± 36.0	0.18 ± 0.06	141.6 ± 51.4	0.19 ± 0.06	43.5
26	2014-10-22	14:28:00	12192	S14E13	X1.6	C	163.3 ± 40.5	0.74 ± 0.23	175.0 ± 37.7	0.79 ± 0.18	53.0
27	2014-10-24	21:41:00	12192	S22W21	X3.1	C	179.1 ± 53.5	1.67 ± 0.43	161.2 ± 16.2	0.94 ± 0.21	73.1
28	2014-11-07	17:26:00	12205	N17E40	X1.6	E	297.5 ± 68.8	4.31 ± 0.51	342.1 ± 70.1	3.86 ± 0.52	4.6
29	2014-12-04	18:25:00	12222	S20W31	M6.1	C	383.0 ± 102.9	0.55 ± 0.12	391.3 ± 37.0	0.58 ± 0.06	11.0
30	2014-12-17	04:51:00	12242	S18E08	M8.7	E	142.9 ± 9.7	4.55 ± 0.62	177.5 ± 6.4	4.50 ± 0.70	20.4
31	2014-12-18	21:58:00	12241	S11E15	M6.9	E	165.0 ± 8.2	4.76 ± 0.26	172.5 ± 7.8	4.62 ± 0.33	8.1
32	2014-12-20	00:28:00	12242	S19W29	X1.8	E	275.0 ± 20.1	5.70 ± 0.72	245.8 ± 10.7	6.63 ± 0.95	5.7
33	2015-03-12	14:08:00	12297	S15E06	M4.2	C	243.0 ± 38.7	1.17 ± 0.19	217.7 ± 28.3	1.32 ± 0.23	5.6
34	2015-06-22	18:23:00	12371	N13W06	M6.5	E	172.5 ± 6.6	8.25 ± 0.43	172.9 ± 7.6	7.32 ± 0.44	6.4
35	2015-06-25	08:16:00	12371	N12W40	M7.9	E	220.8 ± 10.5	6.92 ± 0.44	150.8 ± 8.9	6.90 ± 0.56	8.1
36	2017-09-04	20:33:00	12673	S10W11	M5.5	E	145.8 ± 109.6	0.48 ± 0.29	157.9 ± 106.2	0.36 ± 0.21	15.4
37	2017-09-06	12:02:00	12673	S09W34	X9.3	E	383.3 ± 98.19	22.25 ± 5.39	437.2 ± 133.3	19.75 ± 8.77	6.5

Notes.

[a] Eruptive (E) and confined (C) flares.

[b] Average change in horizontal magnetic field (B_h).
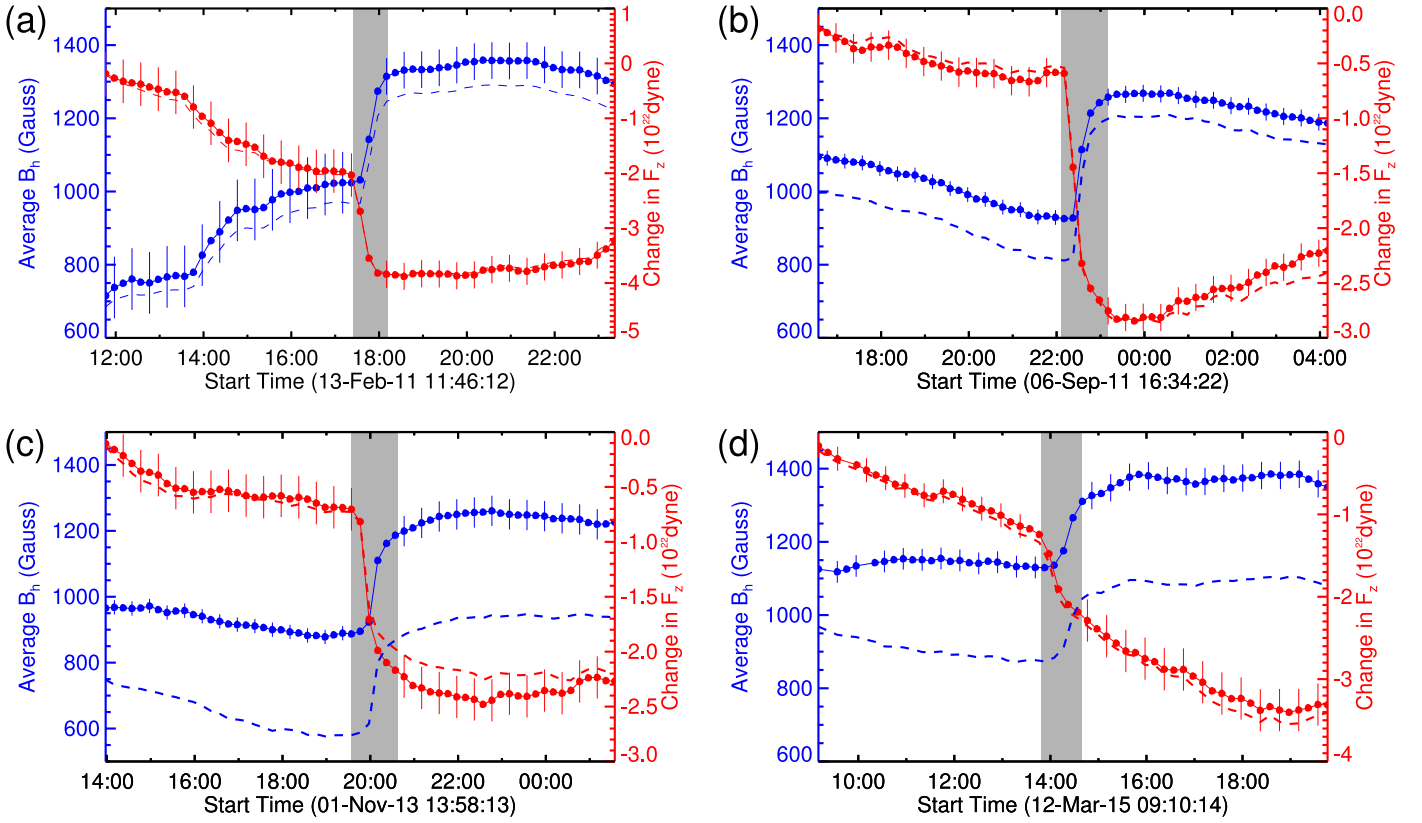
[c] Change in vertical Lorentz force (F_z).

Figure 3. Temporal evolution of average horizontal magnetic field (blue) and vertical Lorentz force (red) calculated by the Lorentz force (solid) and horizontal magnetic field (dashed) contouring method. Panels (a) and (b) represent eruptive events whereas (c) and (d) represent confined ones. The shaded region corresponds to the duration of the change in field. The vertical error bars represent the fluctuations at a 3σ level in both pre- and postflare states.

F_z are the horizontal and vertical components of the Lorentz force calculated over the volume of the AR. The domain $A_{\rm ph}$ corresponds to the photospheric area containing the AR, and dA is the elementary surface area on the photosphere. Similar to the approach by Petrie (2012), we have reversed the signs in Equations (1) and (2) in comparison to Equations (9) and (10) of Fisher et al. (2012). This change accounts for considering the equal and opposite forces acting on the above atmosphere from below. Since significant changes in a horizontal magnetic field and Lorentz forces associated with flares are expected near the PIL (Wang 2006; Petrie & Sudol 2010; Petrie 2012; Sarkar & Srivastava 2018; Sarkar et al. 2019), we focused our analysis on subdomains near the PIL within the flare-producing region of each AR. The reason behind this is based on the assumption that the magnetic field on side boundaries enclosing these subdomains remains relatively constant over time. Additionally, we consider the magnetic field strength on the top boundary to be negligible compared to that at the lower boundary of the photosphere. Consequently, in Equations (1) and (2), only changes in the photospheric magnetic field contribute to the surface integrals, allowing us to estimate the net change in the Lorentz force acting on the photosphere from the volume above the atmosphere.

We developed a semiautomatic tool to select the subregion in which we analyzed the flare-associated changes in Lorentz force for all the events. As the significant changes in Lorentz force are expected to happen very close to the flare peak time, we select time frames approximately 30 minutes before and after the peak phase of the associated flare. Next, we create

difference maps of the horizontal magnetic field and vertical Lorentz force estimated at the above-mentioned time frames separately. We use information on both the horizontal magnetic field (B_h) and vertical Lorentz force (F_z) independently to avoid any selection bias in identifying the areas where the most significant changes occurred as discussed in Petrie (2012), Liu et al. (2022), Vasantharaju et al. (2022), and Yadav & Kazachenko (2023). To these difference maps we apply a threshold to select the subregions that demarcate the area of positive change ($>100\,{\rm G}$) in the horizontal magnetic field or negative change ($<-10^{19}\,{\rm dyn}$) in the vertical component of the Lorentz force. Applying this method, we find several subregions within the AR. In order to find the correct RoI, we manually select the subregion that is nearest the flaring location observed in the AIA images. Figures 1 and 2 illustrate the identified RoIs based on both the B_h and F_z difference maps for the two eruptive and confined events from Table 1 respectively.

3. Results and Discussion

The characteristic variations in the average horizontal magnetic field and the total downward Lorentz force for two eruptive and two confined flaring events that were observed on 2011 February 13 (Event 1), 2011 September 6 (Event 7), 2013 November 1 (Event 16), and 2015 March 12 (Event 33) are described here as examples. Then, for all 37 events, we summarize their variations with flare strength.
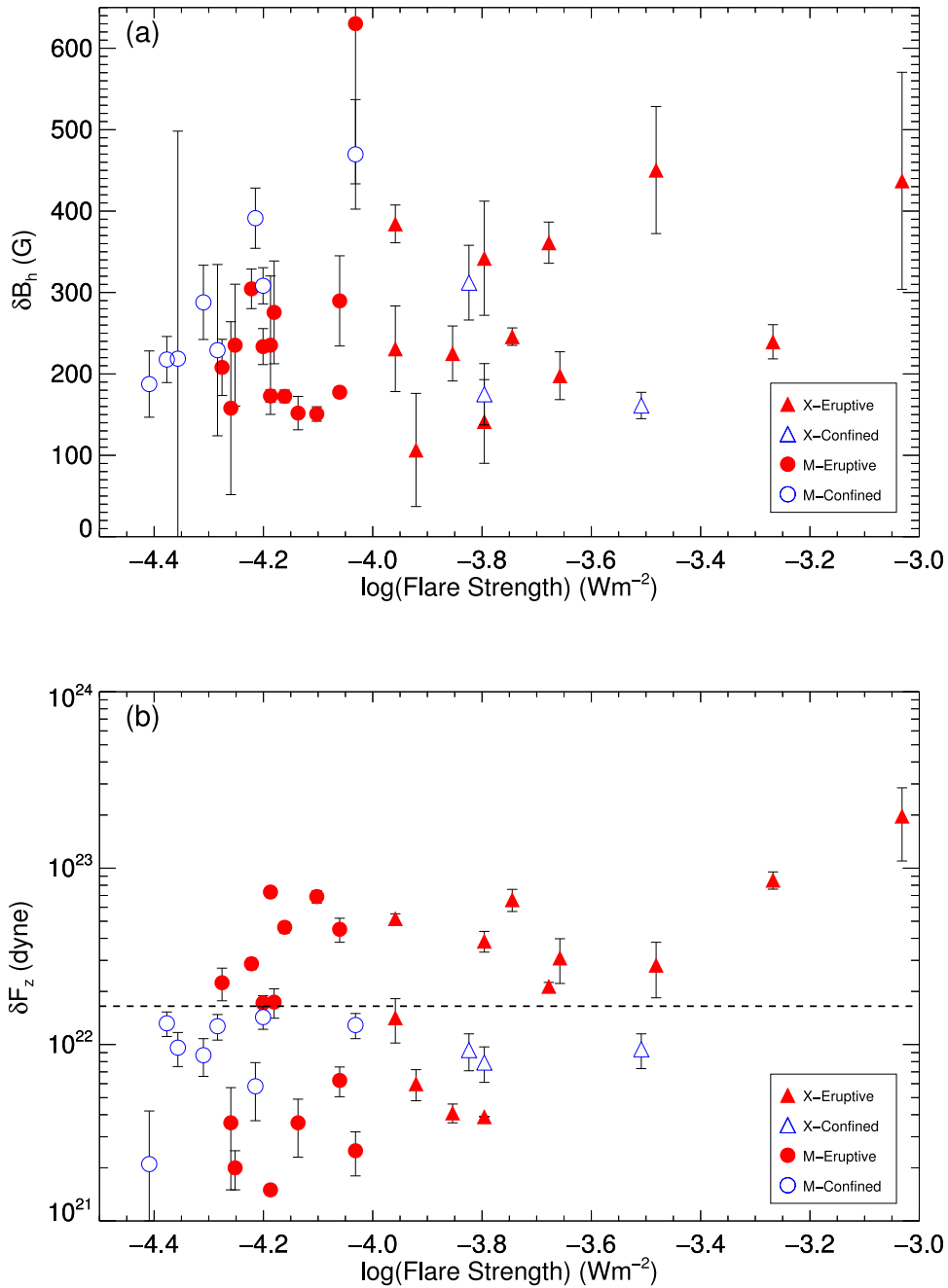
Figure 4. Scatter plots of (a) average change in horizontal magnetic field δB_h vs. logarithmic flare strength and (b) change in vertical Lorentz force δF_z vs. logarithmic flare strength for RoIs identified based on the difference maps of horizontal magnetic field. Filled and empty symbols correspond to eruptive and confined flares, respectively. The triangular and circular symbols are for X-class and M-class flares, respectively. The horizontal dashed line indicates the threshold Lorentz force above which no confined flares are observed.

3.1. Evolution of B_h and F_z

After successful identification of the flaring region using two different methods based on the B_h and F_z difference maps, we continue our analysis within that subregion. We studied the temporal evolution of the average B_h, and the total change in downward Lorentz force, F_z, in the selected region near the PIL for each case. As an example, the time variation of average B_h and downward F_z for the same two eruptive events (Nos 1 and 7) and confined events (Nos 16 and 33) are shown in Figure 3. The top and bottom panels represent the variation of average B_h and downward F_z over time for each eruptive and confined event, respectively. All flaring events show an abrupt change in

both B_h and F_z using both methods. The shaded region in these plots indicates the duration of the change in field. The error bars depict fluctuations corresponding to a 3σ significance in both pre- and postflaring states. These fluctuations are determined through separate linear regression of the temporal changes in B_h and F_z before and after the shaded time interval. The error analysis is performed using a time window of 6 hr and a resolution of 12 minutes in each state. The errors specified in columns 8–11 of Table 1 are determined by averaging the errors from the preflare and postflare states.

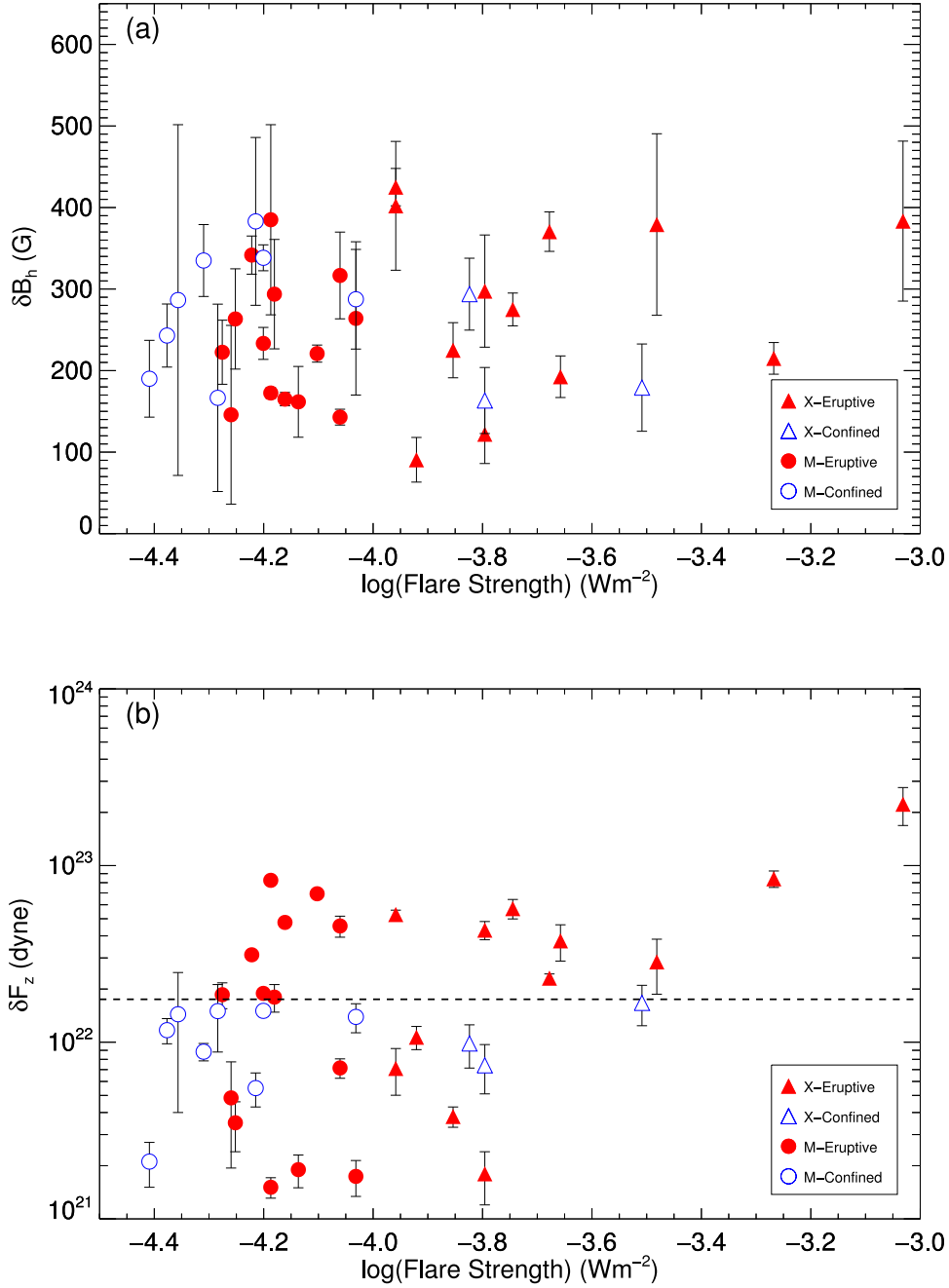Within the RoI determined from the F_z difference maps, the average changes in B_h and F_z for eruptive events as shown in

Figure 5. Similar to Figure 4 but for RoIs identified based on the difference maps of Lorentz force.

Figure 3 are found to be 293.8 G, 1.8×10^{22} dyn for Event 1 and 370.4 G, 2.3×10^{22} dyn for Event 7. Similarly, for confined events, the average changes in B_h and F_z in the RoI given by the change in Lorentz force were 338 G, 1.5×10^{22} dyn for Event 16 and 243 G, 1.2×10^{22} dyn for Event 33.

On the other hand, when the RoI was identified based on the B_h difference map, the average changes in B_h and F_z for eruptive events were 275.1 G, 1.7×10^{22} dyn for Event 1 and 361 G, 2.1×10^{22} dyn for Event 7, respectively. For confined events, the average changes in B_h and F_z in the RoI given by the change in horizontal magnetic field were 308.3 G, 1.4×10^{22} dyn for Event 16 and 217.2 G, 1.3×10^{22} dyn for Event 33.

Figure 3 shows that the enhancement of average B_h is permanent throughout the postflare phase (at least within 6 hr of the time window after the flare peak time), which agrees with the previous studies (Petrie 2012; Wang et al. 2012b; Sun et al. 2017; Liu et al. 2022). The total downward F_z is observed to show an abrupt decrease during the flare interval, which is also irreversible. The average changes in B_h and the total change in vertical F_z for all 37 events, analyzed for different RoI identification methods, are tabulated in Table 1.

3.2. Statistics of B_h and F_z Evolution

In this subsection, we present the statistical properties of the average changes δB_h and δF_z for all the events listed in Table 1. The results show that the average δB_h ranges from 15 G to

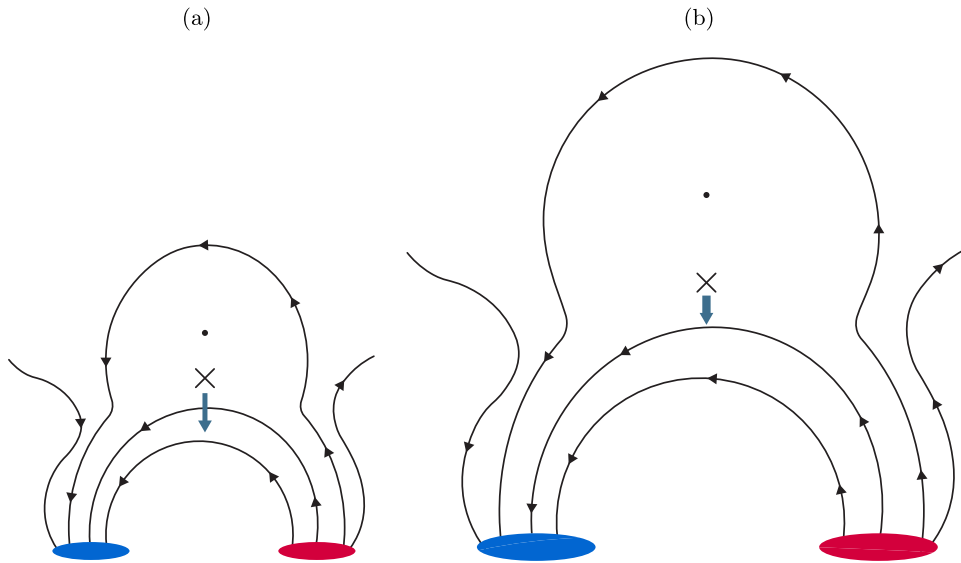(a)   (b)

Figure 6. A sketch of the magnetic field configuration of (a) an eruptive event with greater change in Lorentz force and (b) an eruptive event with smaller change in Lorentz force. Red and blue filled regions are regions of positive and negative polarity whereas solid lines refer to the magnetic field lines. X marks the location of the reconnection site, and the downward arrow implies the direction of vertical Lorentz force responsible for the increase in horizontal magnetic field.

425 G, while the change in Lorentz force varies from 1.5×10^{21} dyn to about 22.3×10^{22} dyn when the RoI was identified based on the change in vertical Lorentz force. Similarly, the average δB_h ranges from 45 G to 630 G, while the change in Lorentz force varies from 1.5×10^{21} dyn to about 19.8×10^{22} dyn when the RoI was identified based on the change in horizontal magnetic field. The data variations result from the adoption of different methods to identify the RoI. This approach was employed to prevent any potential bias in the analysis. However, it is important to note that the results do not show significant differences and remain within the error limits.

Figures 4 and 5 illustrate the changes in average B_h and total downward F_z plotted against the flare strength for the B_h and F_z contouring methods respectively. The change in average B_h does not exhibit statistically significant differences between eruptive and confined events, which is consistent with the findings of Liu et al. (2022) and Yadav & Kazachenko (2023).

However, the change in F_z with flare strength clearly distinguishes between the two types of events. All confined flares have $\delta F_z < 1.8 \times 10^{22}$ dyn, whereas most eruptive flares show higher δF_z values than the above-mentioned limit. This suggests that the strength of flare-associated δF_z depends on whether the flare is eruptive or confined. The threshold limit can serve as a criterion for determining the presence of the associated CMEs based on these calculations. This reveals that while the change in average B_h does not discriminate between eruptive and confined events, the change in total downward Lorentz force provides a clear distinction, indicating that magnetic imprints on the photosphere can be indicative of flare eruptivity.

It is worth noting that nine out of the 26 eruptive events exhibit a change in F_z below the previously mentioned threshold limit. We present one such event in Figures 7(b) and (d). In panel (b), the two green contours represent the regions where the most significant change in Lorentz force is observed. Interestingly, in this event, the strong (>100 G) opposite polarity regions are not in close proximity to each other. This spatial arrangement seems to have an impact on the magnetic field dynamics. On the other hand, the rest of the 17

eruptive flares associated with δF_z greater than the threshold value are observed to occur where the regions of strong opposing polarities are close to each other (see an example of such an event in Figures 7(a) and (c)).

This indicates that the morphology of the active region may be a contributing factor in the relatively smaller change in F_z in our investigation. The spatial distribution of magnetic polarities within the active region appears to play a role in shaping the observed changes in magnetic fields and Lorentz forces during eruptive events.

This can be better understood with the help of a cartoon, as shown in Figure 6. The cartoon illustrates how the spatial distribution and arrangement of opposite polarity regions within an active region can influence the observed changes in magnetic fields and Lorentz force during flaring events. Solar flares are usually observed with two parallel ribbons, lying on both sides of the PIL. If the two flare ribbons are thought of as being connected via newly reconnected semicircular magnetic loops, then the distance between the two parallel ribbons would be proportional to the length of the loop and the reconnection height (Reep & Toriumi 2017; Toriumi et al. 2017). Thus, a shorter ribbon distance would correspond to a smaller loop, and a longer ribbon distance to a larger loop in the solar atmosphere. For those events where the opposite polarity regions are in close proximity, the distance between the two parallel ribbons at the flare onset time is much shorter, as they form nearer to the PIL. This suggests that, in such cases, reconnection initiates at a lower altitude, resulting in a more significant impact on the photosphere characterized by larger changes in the Lorentz force (Liu et al. 2022; Yadav & Kazachenko 2023). However, if the strong opposite polarity regions are not in close proximity to each other, the flare ribbons start a bit away from the PIL, indicating that the reconnection begins at a greater height. As a result, the impact on the solar photosphere is less in this situation, which justifies a smaller change in Lorentz force that we observed.

This explanation is well consistent with the results shown in Figures 7(c) and (d), where the ribbon distance (d_{ribbon}) is estimated at the onset of the associated flares. As the flare
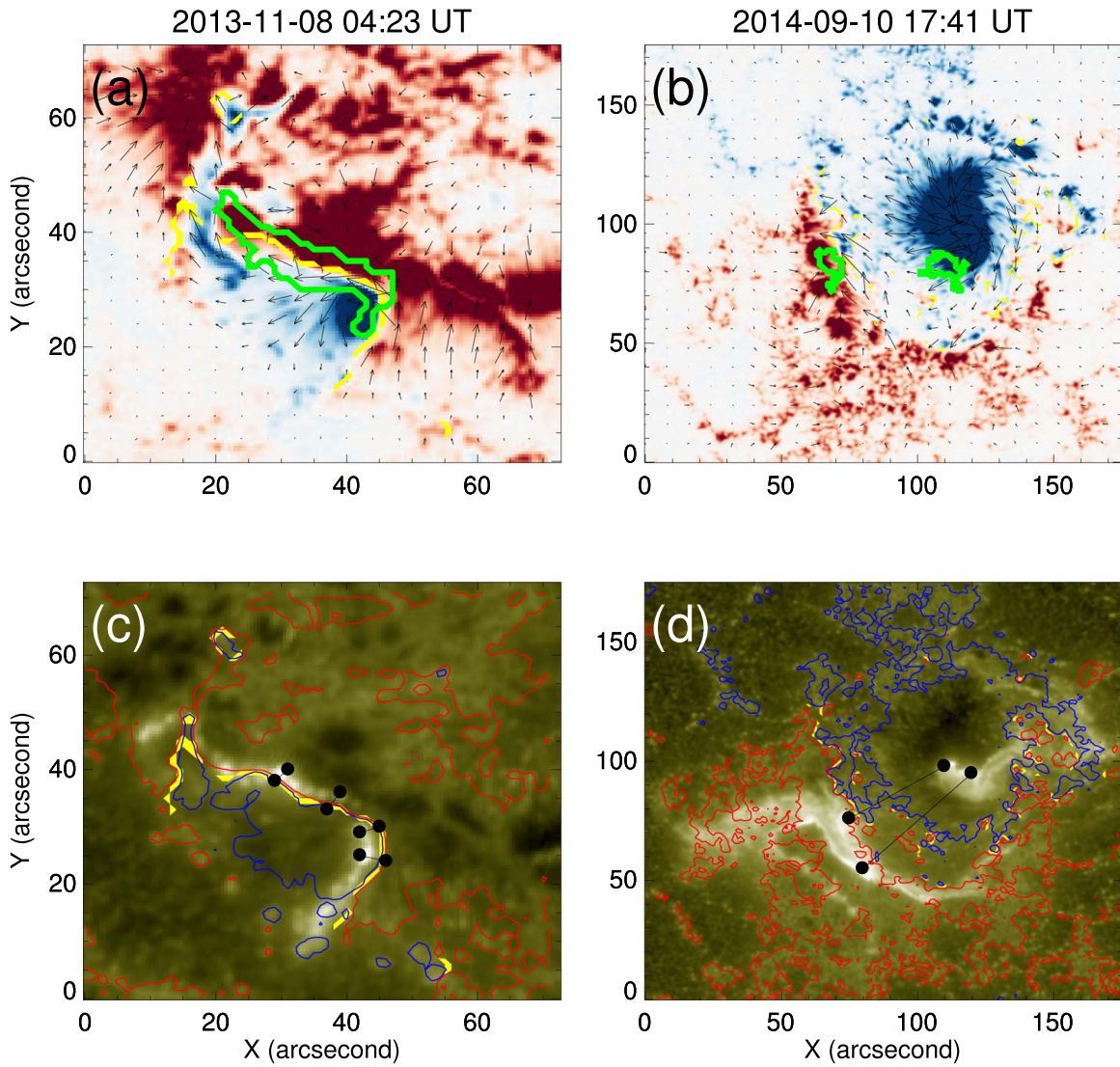
Figure 7. Illustrations demonstrating the calculation of ribbon distances for two events. The top panels represent the photospheric magnetic field maps for the two events that occurred on (a) 2013 November 8 at 04:23 UT and (b) 2014 September 10 at 17:41 UT. The red/blue colors represent the positive/negative polarities of B_z plotted within a range of ± 500 G. The yellow line indicates the PIL and the green contour signifies the region where the significant change in Lorentz force is observed. The black arrows represent the horizontal magnetic field lines. The bottom panels show the corresponding flare ribbons as observed in the AIA 1600 Å channels. The blue and red contours represent the overlaid positive and negative polarities of B_z at levels of ± 100 G. The solid black lines represent the ribbon distances.

ribbons mark the footpoints of the reconnecting magnetic loops, half of the distance ($d_{\mathrm{ribbon}}/2$) between the two flare ribbons estimated at the onset time of the flare serves as a proxy for the initial reconnection height in the solar corona. We use the observations from the AIA 1600 Å channel to identify the flare ribbons as shown in Figure 7.

The method utilized for estimating the ribbon distance (d_{ribbon}) is presented with the example of two flares from our event list as depicted in Figure 7. The first one was the X1.1 eruptive flare that occurred on 2013 November 8 (Event 19) and the second one was the X1.6 eruptive flare that occurred on 2014 September 10 (Event 25). Although both flaring events were eruptive in nature, the change in Lorentz force associated with Event 19 surpasses the critical threshold, whereas that for Event 25 falls below it. In order to understand the distinct morphological differences between these two events, we first identify the proximity of the PIL by superimposing the

contours of B_z at levels of ± 100 G onto the AIA 1600 Å images. Additionally, we apply the automated algorithm to identify the PIL (indicated by the yellow lines) as developed in Sarkar & Srivastava (2018). Figure 7(c) depicts that the flare ribbons at the onset time of the flare for Event 19 form very close to the PIL. Moreover, the associated HMI observations show that the opposite polarity regions of strong B_z are close to each other, forming a compact field region near the flaring PIL. As the flare ribbons at either side of the PIL for Event 19 do not form parallel to each other, we manually selected multiple points on the PIL from which we measured the shortest distance to the ribbon. Furthermore, taking an average of those multiple measurements and multiplying the mean distance by a factor of 2, we estimate the distance d_{ribbon}. In contrast to Event 19, the flare ribbons in Event 25 form much further away from the PIL, and the opposite polarity regions of strong B_z are also located away from the PIL, forming a dispersed field region at the flaring location (see Figures 7(b) and (d)). As the flare
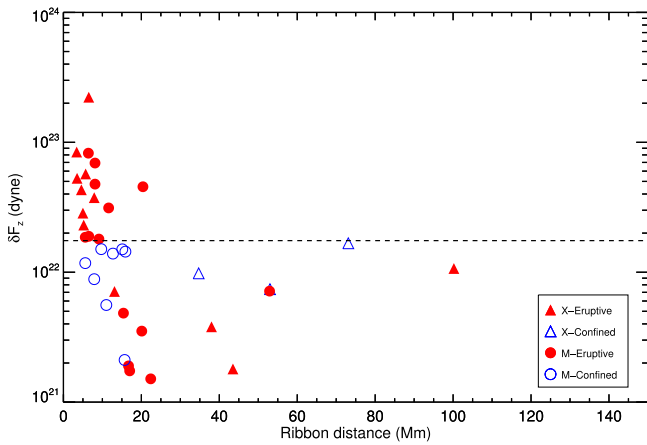
Figure 8. Scatter plot of the change in vertical Lorentz force vs. ribbon distance. The values of the change in Lorentz force shown in the figure are estimated using the method based on the Lorentz force difference maps. Filled and empty symbols correspond to eruptive and confined flares, respectively. The triangular and circular symbols imply X-class and M-class flares, respectively. The horizontal dashed line is drawn to illustrate the threshold value of the change in Lorentz force. Few data points overlap each other.

ribbons in Event 25 form parallel to each other, we select points along the ribbons located either side of the PIL to estimate the average distance (d_{ribbon}) between the two ribbons. We apply the above-mentioned method to all the events and list the estimated d_{ribbon} in Table 1.

The change in Lorentz force is plotted in Figure 8 against d_{ribbon}. It is evident from the plot that the majority of eruptive events exhibit a ribbon separation smaller than 9 Mm.

In contrast, those eruptive events that show a smaller change in the Lorentz force tend to have greater ribbon distances, typically exceeding 15 Mm. This indicates a potential implication between the ribbon separation and the magnitude of the change in Lorentz force during eruptive events. Thus the ribbon separation could serve as an additional factor to consider when studying the magnetic imprints associated with solar flares. Overall, this helps to visualize how the specific morphology of the active region plays a crucial role in determining the magnitude of changes in the total downward Lorentz force (F_z), and this may be one of the factors contributing to the observed variations during such events.

3.3. Downward Propagation of the Lorentz Force

We applied the same procedure as in observational data analysis to the B- and C-class synthetic flare events, and similar profiles of B_h and F_z are observed. Figure 9 presents the results of our analysis performed on the simulation data. Utilizing our semiautomatic code, we are able to select the RoIs accurately (see the green contours in Figures 9(a) and (c)), which agree with the flaring region identified by Korsós et al. (2018) based on the temperature anomaly. The dashed vertical lines in Figures 9(b) and (d) represent the onset times of the B- and C-class flares. The changes in B_h in these flare are 60 G and 400 G, respectively, whereas the changes in F_z are 0.15×10^{22} dyn and 0.27×10^{22} dyn respectively.

We have noticed a remarkable resemblance in the temporal evolution in the simulation with the observational data for the changes in horizontal magnetic field and vertical Lorentz force. While we cannot directly compare the simulation results to our observational data due to differences in flare class and the size of active regions involved, the fact that both the horizontal

magnetic field and Lorentz force display similar variations indicates that the underlying physics governing the changes in magnetic properties remains consistent across different flare classes.

Our simulation allows us to calculate the total Lorentz force, defined by $\boldsymbol{J} \times \boldsymbol{B}$, in a 3D setup. In contrast to observational data, where magnetic field components are only available at the solar surface, our simulation provides all physical variables defined at all heights from the photosphere to the corona. We plotted height versus time for the Lorentz force averaged over the horizontal plane for the two synthetic events as shown in Figure 10, which agrees with the eruption time mentioned in Korsós et al. (2018). This comes out to be of the order of 10^2 dyn whereas the volume integral of average $\boldsymbol{J} \times \boldsymbol{B}$ over the domain comes out of the order of 10^{22} dyn, which agrees with the observational results. We observed that the Lorentz force propagates toward the photosphere from the reconnection site similar to Barczynski et al. (2019). The average propagation speed is $2.4 \mathrm{~km~s}^{-1}$ and $2.3 \mathrm{~km~s}^{-1}$ for simulated B- and C-class flares, respectively. Therefore, we argue that the Lorentz force from the reconnection site (marked "X" in Figure 6) propagates downward toward the photosphere, resulting in changes in F_z and B_h as estimated from the HMI magnetogram.

Our analysis of the synthetic flare events provides further support for the importance of the downward propagation of the Lorentz force and its influence on the photosphere, which is consistent with both previous simulation studies and the observational data.

4. Summary

We present a statistical analysis of the flare-associated changes in the photospheric magnetic field close to the neutral line of the flaring region during the 37 flare events stronger than a GOES M5 class flare from 26 different ARs. We used a semiautomatic technique to select the subregion close to the PIL where the significant changes in Lorentz force occur during the flare. We investigate whether the flare-associated changes in Lorentz force and the photospheric magnetic field have any dependence on the confined or eruptive nature of a flare.

We have found a consistent pattern in the variation of the change in horizontal photospheric magnetic field (B_h) and the change in vertical Lorentz force (F_z) for each event using two different methods to identify the most significant change in field. The mean B_h appears to increase in every case, showing abrupt enhancement in the temporal evolution. The observed increase in the horizontal magnetic field, B_h, can be attributed to the coronal implosion conjecture, as proposed by Hudson (2000), or reconnection-driven contraction in postflare loops, as shown by Barczynski et al. (2019) using an MHD simulation with zero-β approximation.

We also observed a significant, abrupt, permanent downward change in vertical Lorentz force during each flare, demonstrating an abrupt change in the temporal evolution, which is a common feature in large flares (Sun et al. 2012; Wang et al. 2012a). To understand this behavior, we compared it with the results of the MHD simulation of a solar flare and found that the Lorentz force ($\boldsymbol{J} \times \boldsymbol{B}$) propagates downward toward the photosphere over time, leading to the observed change in vertical Lorentz force. We observed similar temporal evolution profiles for the average δB_h and the total δF_z for both of these synthetic flares. This consistency in the temporal evolution
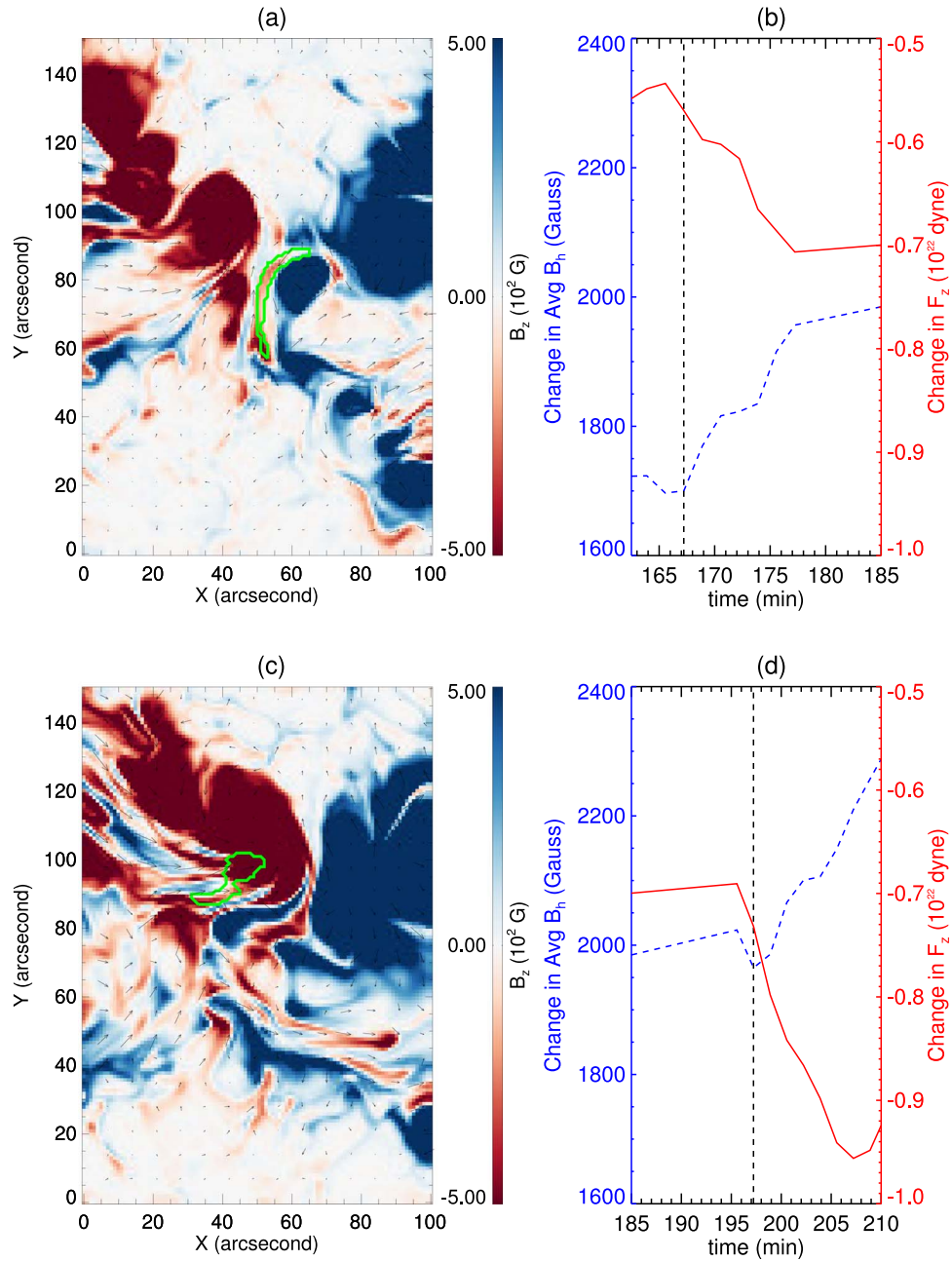
Figure 9. (a) Illustration of the vertical magnetic field B_z for the B-class synthetic flare events and (b) the corresponding temporal evolution of average horizontal magnetic fields (blue) and vertical Lorentz force (red). (c), (d) Same as (a) and (b) but for the synthetic C-class flare. The green contours in (a) and (c) mark the region where significant change in Lorentz force occurs. The strength of the vertical magnetic field is represented by the color bar. The dashed vertical black lines represent the flare time.

patterns of δB_h and δF_z further supports the robustness and validity of our method of analysis for studying flares, both in observational data and in simulated events.

Our conclusion regarding the distinction between eruptive and confined flares is based on a comparison of δF_z (the change in vertical Lorentz force) for the two types of flares. Eruptive flares were found to leave a significant magnetic imprint on the solar photosphere. Conversely, confined flares exhibited comparatively smaller changes in the photospheric magnetic field (Sun et al. 2012; Sarkar & Srivastava 2018). This observation is in agreement with the flare-related momentum balance condition, which suggests that the impulse from the Lorentz force is directly related to the associated CME

momentum (Fisher et al. 2012; Wang et al. 2012b). This is strongly supported by our findings from the analysis of the selected 26 eruptive and 11 noneruptive flares in this work. The significant change in the photospheric magnetic field for eruptive flares and the comparatively smaller change for confined flares support the notion that the impulse from the Lorentz force is linked to the presence and strength of associated CMEs.

However, to distinguish between the two types of flares, our analysis offers an upper threshold value of the change in vertical Lorentz force. Despite nine eruptive events having a change in Lorentz force below our threshold, we did not witness any confined events with Lorentz force larger than
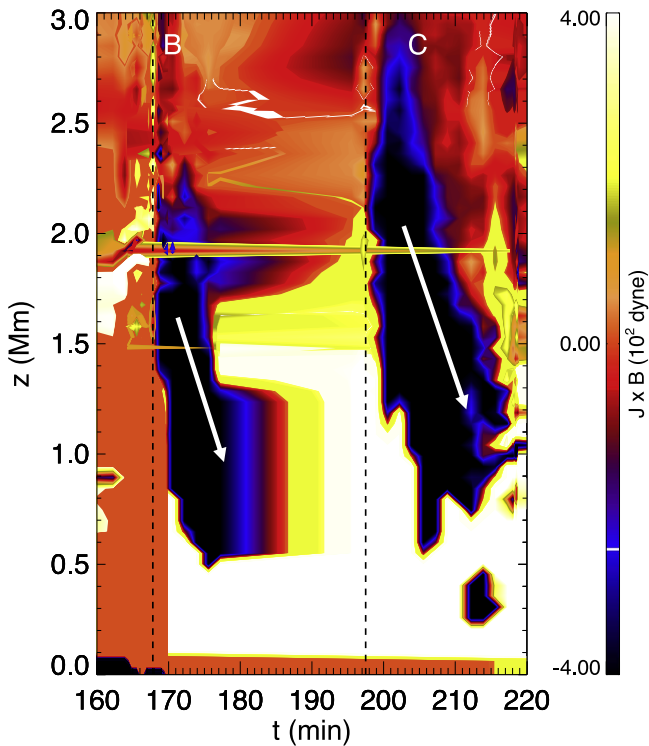
Figure 10. Height–time diagram of Lorentz force from the 3D MHD simulation to show its downward propagation. The dashed vertical lines represent the time of the two synthetic flares. The arrow is to guide the eye toward the propagation direction of the Lorentz force.

1.8×10^{22} dyn. Using 21 flaring episodes, between 2010 August and 2015 November, Vasantharaju et al. (2022) suggested that the strength of the magnetic imprint is independent of whether the flare is eruptive or not. In contrast, our findings indicate that the mean change in B_h makes no distinction, whereas the change in vertical Lorentz force provides a clear differentiation between confined and eruptive flares. This difference is likely due to the inclusion of the term δB_z^2 when computing δF_z, identification of the RoI using an improved algorithm, and the inclusion of a larger sample of flaring events in our study with energies equal to or exceeding those of M-class flares.

For eruptive events with a change in Lorentz force below the threshold, we noticed a significantly greater separation between the parallel flare ribbons when they form at the onset time of the flare. The source location of those events also displays distinct morphology, as the distance between the two regions of strongly opposing magnetic polarity at the flaring location is observed to be comparatively larger. This larger separation is due to a greater reconnection height at the start of the flare as compared to the other eruptive events, leading to a weaker change in Lorentz force in the photosphere. Overall, our analysis reveals that the change in the vertical Lorentz force plays a crucial role in distinguishing confined and eruptive flares. The observed differences are influenced by factors such as the CME association and the separation of the parallel flare ribbons at the time of flare onset.

In this paper, we have examined the effects of major flares on fields near neutral lines. The present analysis is a step forward to distinguishing eruptive and confined flares in terms of the change in the vertical Lorentz force. Although a clear distinction between confined and eruptive events has been seen

in this sample, it will be instructive to look at a larger sample of events and their corresponding vector field measurements from HMI and their associations with CMEs.

ORCID iDs

Samriddhi Sankar Maity ⓘ https://orcid.org/0009-0005-4347-9044
Ranadeep Sarkar ⓘ https://orcid.org/0000-0001-6457-5207
Piyali Chatterjee ⓘ https://orcid.org/0000-0002-0181-2495
Nandita Srivastava ⓘ https://orcid.org/0000-0002-0452-5838

References

Andrews, M. D. 2003, SoPh, 218, 261
Aulanier, G. 2016, NatPh, 12, 998
Baker, D. N., Daly, E., Daglis, I., Kappenman, J. G., & Panasyuk, M. 2004, SpWea, 2, S02004
Barczynski, K., Aulanier, G., Masson, S., & Wheatland, M. S. 2019, ApJ, 877, 67
Borrero, J. M., Tomczyk, S., Kubo, M., et al. 2011, SoPh, 273, 267
Carmichael, H. 1964, Proc. of the AAS-NASA Symp. 50, The Physics of Solar Flares, ed. W. N. Hess, (Washington, DC: NASA), 451
Castellanos Durán, J. S., Kleint, L., & Calvo-Mozo, B. 2018, ApJ, 852, 25
Chatterjee, P., Hansteen, V., & Carlsson, M. 2016, PhRvL, 116, 101101
Chen, J. 2017, PhPl, 24, 090501
Fisher, G. H., Bercik, D. J., Welsch, B. T., & Hudson, H. S. 2012, SoPh, 277, 59
Fletcher, L., & Hudson, H. S. 2008, ApJ, 675, 1645
Gosain, S. 2012, ApJ, 749, 85
Green, L. M., Török, T., Vršnak, B., Manchester, W., & Veronig, A. 2018, SSRv, 214, 46
Harrison, R. A. 2003, AdSpR, 32, 2425
Hirayama, T. 1974, SoPh, 34, 323
Hudson, H. S. 2000, ApJL, 531, L75
Hudson, H. S., Fisher, G. H., & Welsch, B. T. 2008, in ASP Conf. Ser. 383, Subsurface and Atmospheric Influences on Solar Activity, ed. R. Howe et al. (San Francisco, CA: ASP), 221
Jing, J., Liu, C., Lee, J., et al. 2018, ApJ, 864, 138
Kazachenko, M. D. 2023, ApJ, 958, 104
Kazachenko, M. D., Albelo-Corchado, M. F., Tamburri, C. A., & Welsch, B. T. 2022, SoPh, 297, 59
Kleint, L. 2017, ApJ, 834, 26
Kopp, R. A., & Pneuman, G. W. 1976, SoPh, 50, 85
Korsós, M. B., Chatterjee, P., & Erdélyi, R. 2018, ApJ, 857, 103
Korsós, M. B., Ludmány, A., Erdélyi, R., & Baranyi, T. 2015, ApJL, 802, L21
Kumar, H., & Kumar, B. 2020, MNRAS, 497, 976
Lemen, J. R., Title, A. M., Akin, D. J., et al. 2012, SoPh, 275, 17
Li, Y., Jing, J., Fan, Y., & Wang, H. 2011, ApJL, 727, L19
Liu, L., Zhou, Z., Wang, Y., Sun, X., & Wang, G. 2022, ApJL, 934, L33
Moore, R. L., Sterling, A. C., Hudson, H. S., & Lemen, J. R. 2001, ApJ, 552, 833
Pencil Code Collaboration, Brandenburg, A., & Johansen, A. 2021, JOSS, 6, 2807
Pesnell, W. D., Thompson, B. J., & Chamberlin, P. C. 2012, SoPh, 275, 3

Petrie, G. J. D. 2012, ApJ, 759, 50
Petrie, G. J. D. 2019, ApJS, 240, 11
Petrie, G. J. D., & Sudol, J. J. 2010, ApJ, 724, 1218
Reep, J. W., & Toriumi, S. 2017, ApJ, 851, 4
Sammis, I., Tang, F., & Zirin, H. 2000, ApJ, 540, 583
Sarkar, R., Pomoell, J., Kilpua, E., et al. 2024, APJS, 270, 18
Sarkar, R., & Srivastava, N. 2018, SoPh, 293, 16
Sarkar, R., Srivastava, N., & Veronig, A. M. 2019, ApJL, 885, L17
Schou, J., Scherrer, P. H., Bush, R. I., et al. 2012, SoPh, 275, 229
Shibata, K., & Magara, T. 2011, LRSP, 8, 6
Siscoe, G. 2000, JASTP, 62, 1223
Sturrock, P. A. 1966, Natur, 211, 695
Sudol, J. J., & Harvey, J. W. 2005, ApJ, 635, 647
Sun, X., Hoeksema, J. T., Liu, Y., Kazachenko, M., & Chen, R. 2017, ApJ, 839, 67
Sun, X., Hoeksema, J. T., Liu, Y., et al. 2012, ApJ, 748, 77
Toriumi, S., Schrijver, C. J., Harra, L. K., Hudson, H., & Nagashima, K. 2017, ApJ, 834, 56
Toriumi, S., & Wang, H. 2019, LRSP, 16, 3
Turmon, M., Jones, H. P., Malanushenko, O. V., & Pap, J. M. 2010, SoPh, 262, 277
Vasantharaju, N., Vemareddy, P., Ravindra, B., & Doddamani, V. H. 2022, ApJ, 927, 86
Wang, H. 2006, ApJ, 649, 490
Wang, H., & Liu, C. 2015, RAA, 15, 145
Wang, S., Liu, C., Liu, R., et al. 2012a, ApJL, 745, L17
Wang, S., Liu, C., & Wang, H. 2012b, ApJL, 757, L5
Webb, D. F., & Howard, T. A. 2012, LRSP, 9, 3
Wheatland, M. S., Melrose, D. B., & Mastrano, A. 2018, ApJ, 864, 159
Wiegelmann, T., Thalmann, J. K., & Solanki, S. K. 2014, A&ARv, 22, 78
Yadav, R., & Kazachenko, M. D. 2023, ApJ, 944, 215
Yang, Y.-H., Hsieh, M.-S., Yu, H.-S., & Chen, P. F. 2017, ApJ, 834, 150
Yashiro, S., & Gopalswamy, N. 2009, IAU Symp. 257, Universal Heliophysical Processes, ed. N. Gopalswamy & D. F. Webb, (Cambridge: Cambridge Univ. Press), 233
Yashiro, S., Gopalswamy, N., Akiyama, S., Michalek, G., & Howard, R. A. 2005, JGRA, 110, A12S05
Youssef, M. 2012, JAsGe, 1, 172
Zhang, J., Dere, K. P., Howard, R. A., Kundu, M. R., & White, S. M. 2001, ApJ, 559, 452
Zirin, H., & Liggett, M. A. 1987, SoPh, 113, 267